Pergamon

0301-9322(94)E0020-J

Int. J. Multiphase Flow Vol. 20, No. 5, pp. 915–926, 1994

0301-9322/94 $7.00 + 0.00

ULTRASONIC IMAGING VELOCIMETRY OF TRANSIENT LIQUEFACTION OF COHESIONLESS PARTICULATE MEDIA

H. K. KYTÖMAA and S. W. CORRINGTON

Department of Mechanical Engineering, Massachusetts Institute of Technology, Cambridge, MA 02139, U.S.A.

(Received 15 June 1992; in revised form 24 February 1994)

Abstract—The loss of shear strength of a water-saturated cohesionless particle bed, known as liquefaction, was imaged in real time using clinical ultrasound back-scattering in an effort to distinguish liquefied from settled states in transient events. In the ultrasonic movies, the liquefied regions were found to be readily identifiable by their characteristic small-scale random fluctuations, which are consistent with the known phenomenon of particle diffusion in suspensions. The time sequences were analyzed and found to display an upward propagating interface separating settled from suspended regions, similar to the kinematic waves that arise in batch sedimentation, although their speeds were measured to be up to an order of magnitude greater than the terminal velocity of an isolated particle. On the basis of this similarity, the solidification process that follows liquefaction was modeled using drift flux theory and the Richardson–Zaki correlation, which was found to give a good match with the high measured solidification wave speeds.

1. INTRODUCTION

This study was undertaken to demonstrate the capabilities of clinical ultrasonic imaging for suspensions, slurries and porous media applications. The demanding task of imaging a cohesionless particle assembly that suddenly loses its shear strength through the process of liquefaction was chosen as an example of a process that has not been successfully monitored with any other technique. Liquefied and solidified states are difficult to distinguish due to the small difference in solids fraction that differentiates them. A good review of the phenomenon of liquefaction is given by the National Research Council (1985). The liquefied state is typically characterized through a secondary indicator, namely a rise in the pore pressure gradient which implies that the particulate medium no longer supports itself in a static sense, but is in suspension and is supported by the fluid. In the solidified state, also called the settled state, the particle matrix supports its own buoyant weight. A liquefied medium will flow in response to applied shear stresses, while the solidified state is able to sustain finite shear stresses without appreciable deformation.

Various techniques have been used to study sedimentation processes. In the settling of dilute suspensions, light absorption has proven quite effective, while nuclear magnetic resonance (NMR) imaging (Turney 1990) and X-ray computer aided tomography (Auzerais *et al.* 1988, 1990) have both been utilized with denser mixtures which are not readily penetrated by light. In these, the concentration resolution has been of the order of 1% at best, while liquefaction involves concentration changes of as little as 0.1%, which cannot be discerned with any of these techniques. As ultrasonic methods interrogate the mechanical properties of the test material, it was speculated that such a method would be appropriate for the present application.

In this paper, consecutive liquefaction/solidification events of a cohesionless saturated bed of non-Brownian 50 μm glass spheres were ultrasonically imaged. Ultrasonic image features are described and discussed in section 2. The speed of internal settling waves was measured and shown to be much larger than typical values associated with dilute systems. Visual batch sedimentation tests with the same apparatus and particles are described in section 3, identifying the similarities and differences between these two processes. In section 4, the drift flux model is used with the Richardson–Zaki (1954) correlation to show that both the batch sedimentation and liquefaction/solidification processes can accurately be described with this simple model. Closing remarks are

presented in section 5 on the potential of ultrasonic imaging in suspensions, slurries and porous media.

2. LIQUEFACTION/SOLIDIFICATION EXPERIMENTS

2.1. The flow cell

The 5 × 5 cm acrylic square test section or "phantom" shown in figure 1, was constructed to conduct liquefaction experiments and also to allow the mixtures to be fluidized to prescribed concentrations with an upward water flow. The column is approx. 22 cm high, with an internal cross-sectional area of 19.36 cm^2. During fluidization, water is introduced at an opening at the bottom of the column, and exits through a similar opening at the top. The particles were 50 μm glass spheres with a density of 2.27 g/cm^3, and were supported at the bottom of the column by a 6 mm porous plate (Porex polypropylene with a characteristic pore size of 100 μm), which also acts as a flow distributer.

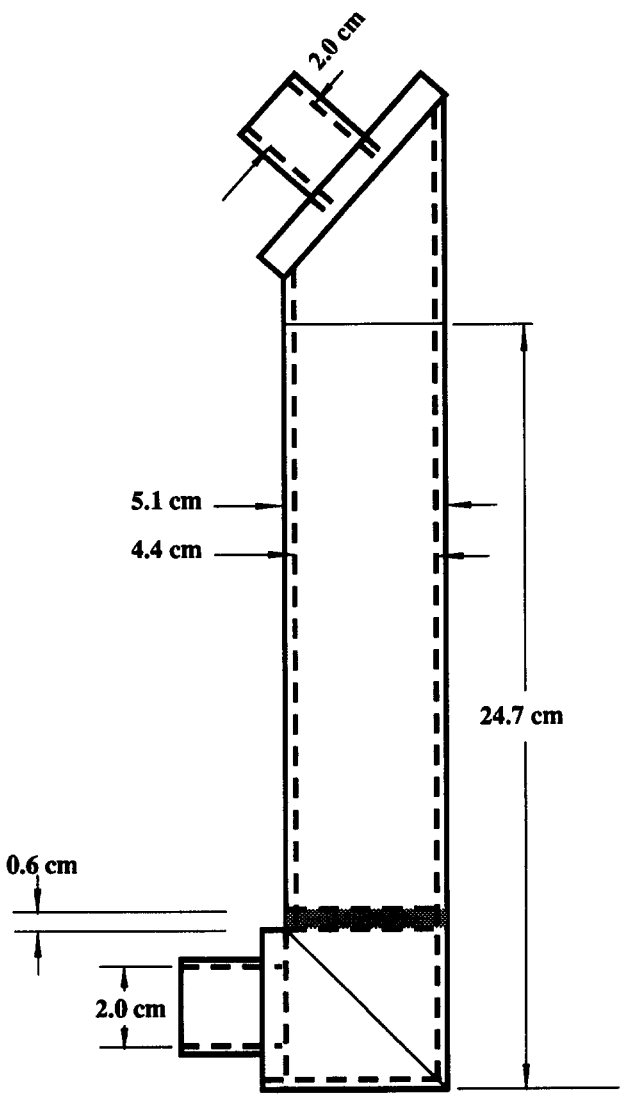

Figure 1. Schematic of the acrylic test section used for fluidization, sedimentation and liquefaction experiments. A 6 mm porous polypropylene plate of 100 μm pore size supports the beads and acts as a flow straightener for fluidization tests. The internal dimensions are nominally 5 × 5 cm and the walls are 3 mm thick. Hoses directly attach to the inlet and exhaust nipples.

2.2. Description of the operation of the ultrasonic back-scattering system

The system used for these experiments (Hewlett–Packard Sonos 1000) uses a transducer that constitutes a phased array of 128 active ultrasonic elements that are each focused in the direction perpendicular to the imaging plane with an acoustic lens. A brief description of the operation of this device is given below, but the interested reader is referred to Geiser (1988) or the Hewlett–Packard manual of this machine for further information.

During one viewing sequence, 121 beams are created to view a 90° pie-shaped region as shown in figure 2, and 30 such images can be created in a second. Each beam is created using all elements operating as a phased array. By using all elements the quality of each beam is superior to the beam emanating for an individual element. Such steered beams are created by firing a short critically damped pulse (duration $\approx 1\ \mu s$) from all elements with the appropriate phase delays to achieve constructive interference along the desired line. After the steered beam is created, the transducer immediately switches to the listening mode to receive echoes from scatterers. Reception also operates in a phase discriminating fashion to detect echoes along the intended line alone. The reconstructed received signal is translated into gray scale information and the time scale is translated into distance along the line that corresponds to the steered beam. Thus a linear gray scale image can be formed of reflecting boundaries and scatterers along a line that corresponds to the steered beam. This phased array sequence is carried out 121 times to sweep the 90° pie. As the beams are arranged in a fan, it is convenient to define a radial dimension along the direction of the ultrasonic beams, and a tangential dimension perpendicular to these. The temporal resolution of this type of system is less than a microsecond, and spatial features smaller than 1 mm can readily be discerned in the radial direction. But as the spacing of these beams increases outwards, the tangential resolution is poorer, and the gray scale values are linearly interpolated between beams. At a distance of 5 cm from the transducer, the resolution is typically of the order of 1 mm.

Transducers of various natural frequencies are available from 2.5 MHz upward. For clinical applications, the lower frequencies are used when deeper penetration is needed. In the present experiments, it is also necessary that the signal strength remains sufficiently high across the full width of the 5 cm test section.

2.3. Frequency considerations

In glass–water systems transition from the long wavelength regime into the multiple scattering regime occurs at a dimensionless frequency, $ka \approx O(1)$, where $k = 2\pi f/c$, f = frequency, c = phase speed in the liquid and a = particle radius. The multiple scattering regime has characteristically high attenuation, and as the objective of this study is to image the interior of saturated particulate materials, adequate penetration is needed. The multiple scattering regime can satisfactorily be avoided with $ka \leqslant 0.4$. With $a = 25\ \mu m$, this corresponds to $f \leqslant 2$ MHz. At 2 MHz the penetration depth into the 50 μm glass sphere suspension near maximum packing is of the order of 10 cm (Atkinson & Kytömaa 1992, 1993), which is ample for our application.

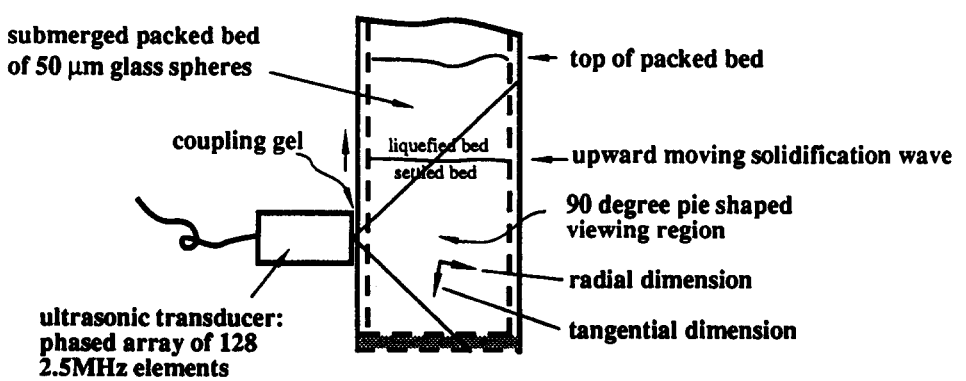

Figure 2. Diagram of the operation of the ultrasonic transducer showing the pie-shaped viewing region.

As a result of the above considerations, and due to the discrete number of available transducer frequencies, a 2.5 MHz MP cardiovascular imaging transducer was adopted. This transducer was used with the HP Sonos 1000 mainframe which displays 30 VHS video images per second.

The ultrasonic transducer was oriented vertically to image a vertical plane through the test section. The transducer was attached to the side of the flow tube approx. 5 cm above the porous plate at the bottom of the phantom, and imaging was conducted through the 3 mm acrylic wall which has an ultrasonic impedance ($z \approx 3.0 \times 10^6$ kg/m^2 s) that is very near that of the saturated particle bed in a random close packed configuration. As a result, no significant artifacts were expected nor observed, although the difference in z between the present materials and biological tissue may cause some distortion in the ultrasonic image. This is discussed below and in appendix A where a dynamic calibration scheme is presented to correct for this. In all cases, a distinct reflection off the back wall of the square section served as evidence of satisfactory penetration.

2.4. Mechanically-induced liquefaction

To ensure repeatable conditions prior to each sequence of liquefaction tests, the particles were fluidized to an approximate solids fraction of 30% and allowed to settle under gravity, after which the bed height was noted and liquefaction tests were started. All tests were imaged ultrasonically. Liquefaction was induced with a hand delivered sharp blow of a metal object to the mixture container. As the settled bed of particles experiences this excitation impulse, the associated pressure overcomes the frictional forces between particles, and for a brief period in time, the particles are no longer supported by the network of particle–particle contacts. As the contacts are broken, the fluid now supports the particles. This manifests itself in an increase in the liquid static pressure from its initial hydrostatic value to the higher value associated with the mixture density. Under the effect of gravity, the particles settle downwards to a denser state.

Each blow resulted in visible compaction of the bed. The bed consistently began to drop immediately after the blow, and assumed its final height after a short period of gradually decreasing height. The resulting change in bed height was measured. This was repeated several times until the bed was no longer observed to compact. Two such series of measurements were made, each consisting of the initial fluidization to 30% solid fraction, followed by the sequence of taps, which were maintained as consistent as possible. During each of these series the bed underwent gradual compaction from an initial solids fraction of ≈ 0.6 to a final value near 0.65. Each decrement in bed height was observed to decrease until compaction fully ceased upon striking. The bed was imaged in real time for each strike. An example of a sequence of images is shown in figure 3 which shows the rise of a distinct interface which separates two regions of markedly different temporal character. The region below appears "frozen", while the upper region is typified by small-scale random fluctuations in the visible texture. This image was created using a moving difference between video images spaced by six frames. By means of this algorithm which highlights temporal changes, the "frozen" settled state appears uniformly grey corresponding to unchanged states between frames, while the liquefied state exhibits characteristic dark and bright tones associated with its fluctuational nature. At the moment the bed is tapped, the image flashes as the receivers are saturated by the sound of the tap. This is followed by the passage of the upward wave. It is interesting to note that the typical length scale that can be discerned in the liquefied region is of the order of 2 mm which is 3–4 wavelengths or 40 particle diameters. This suggests that particles in this system tend to interact in clusters or mechanical entities that have a linear dimension of 40 particle diameters.

3. RESULTS AND ANALYSIS

3.1. Interfacial speeds

The speed of the ultrasonically visible rising interface was determined from the image sequence off a video monitor. For each liquefaction event, the location of the interface was determined visually for two frames, one shortly after the wave becomes visible in the lower part of the image and the other when the wave is near the top of the image. The time separating the two frames was noted. The measurements of the distance traveled by the wave were based on the linear scale

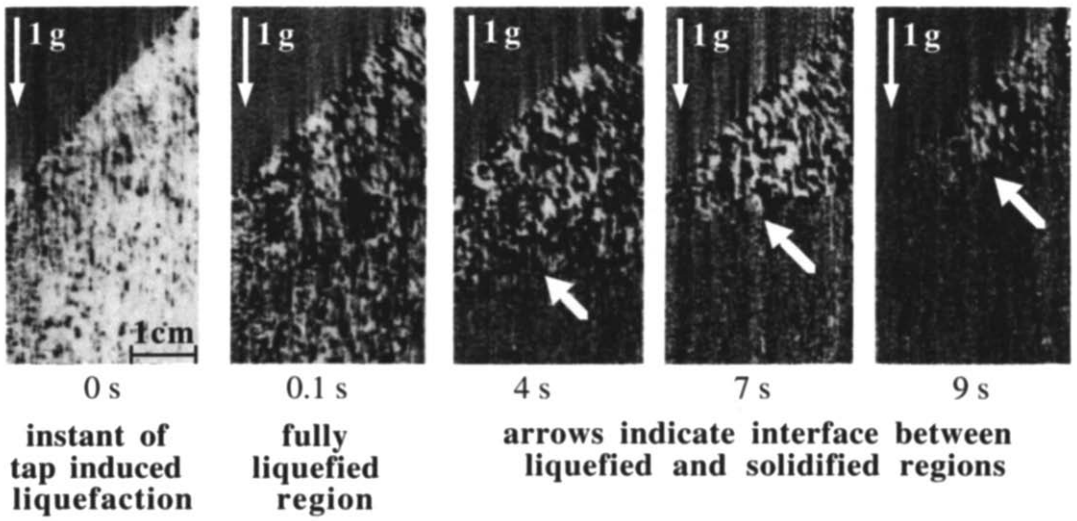

Figure 3. Image of liquefaction event created using a medical ultrasonic system operating at a frequency of 2.5 MHz with 50 μm glass particles in water. This was created with a running subtraction of the image at time ($t - 0.2$ s) from the one at time t to highlight changes in the image. Thus, the stagnant settled state appears uniformly gray, while the liquefied state exhibits characteristic dark and bright tones associated with its fluctuational nature. At the moment the bed is tapped, the image flashes and the passage of the upward wave follows as a clear rising interface (arrow) associated with the growing resettled layer. The diagonal demarkation is the edge of the "pie"-shaped viewing region shown in figure 2.

provided by the instrument, which is used in clinical measurements of the size of internal organs and body parts. While this scale may be accurate or at least consistent for biological tissue, it cannot be expected to hold for the present mixture of glass and water, which has a markedly different sound speed, and hence a different ultrasonic impedance. As a result, refraction at the interface of the transducer may result in a geometrical deformation of the ultrasonic image. To address this issue, a dynamic calibration procedure was developed to determine a single calibration factor to correctly rescale the measured interfacial speeds (this procedure is described in appendix A). The raw and the adjusted speeds are presented in figure 4(a) and (b).

Both sequences of liquefaction events display a distinct and dramatic rise in the wave speed as the solids fraction increases above 0.6. This was evident in the ultrasonic video sequences, until the waves could no longer be seen. It is unclear whether liquefaction ceases to occur or the waves were too fast to be seen at the highest solids fraction due to the quality of the ultrasonic image, although the bed ceased to compact at a solids fraction of about 0.65.

The internal wave speeds are also shown for low initial concentrations created by fluidizing the bed. In these cases, the final concentration was found to be $0.61(\pm 0.005)$ and the internal wave speed fell in the narrow range of $0.032 - 0.038$ cm/s, which is significantly smaller than the ultrasonically determined results, and about 1/3 of the terminal velocity of an isolated particle ($= 1.73$ mm/s). These values therefore support the notion that sedimentation waves typically travel at speeds that are of the order of the terminal velocity of an isolated particle. In contrast, figure 4(a) and (b) shows a singular growth as the packing concentration approaches its maximum attainable value of 0.65. The highest unadjusted speeds were measured to be approximately one order of magnitude higher than the terminal velocity.

3.2. Prediction of the internal sedimentation wave speed

The above ultrasonic experiments reflect a behavior in liquefaction/resolidification that strongly resembles batch sedimentation (see, for example, Wallis 1969). The process of batch sedimentation in which non-Brownian particles settle out of a uniform suspension under the effect of gravity can be described in terms of a rising interface between the settled material and the suspension, and a falling interface between the suspension and the pure fluid, as was first shown by Kynch (1952). When these two interfaces meet, the suspension is fully settled. In non-Brownian sedimentation, bed elasticity may lead to its compression of the settled mass under its own weight, as has been shown by Terzaghi (1943) and Tiller (1981), and irreversible particle rearrangement may occur

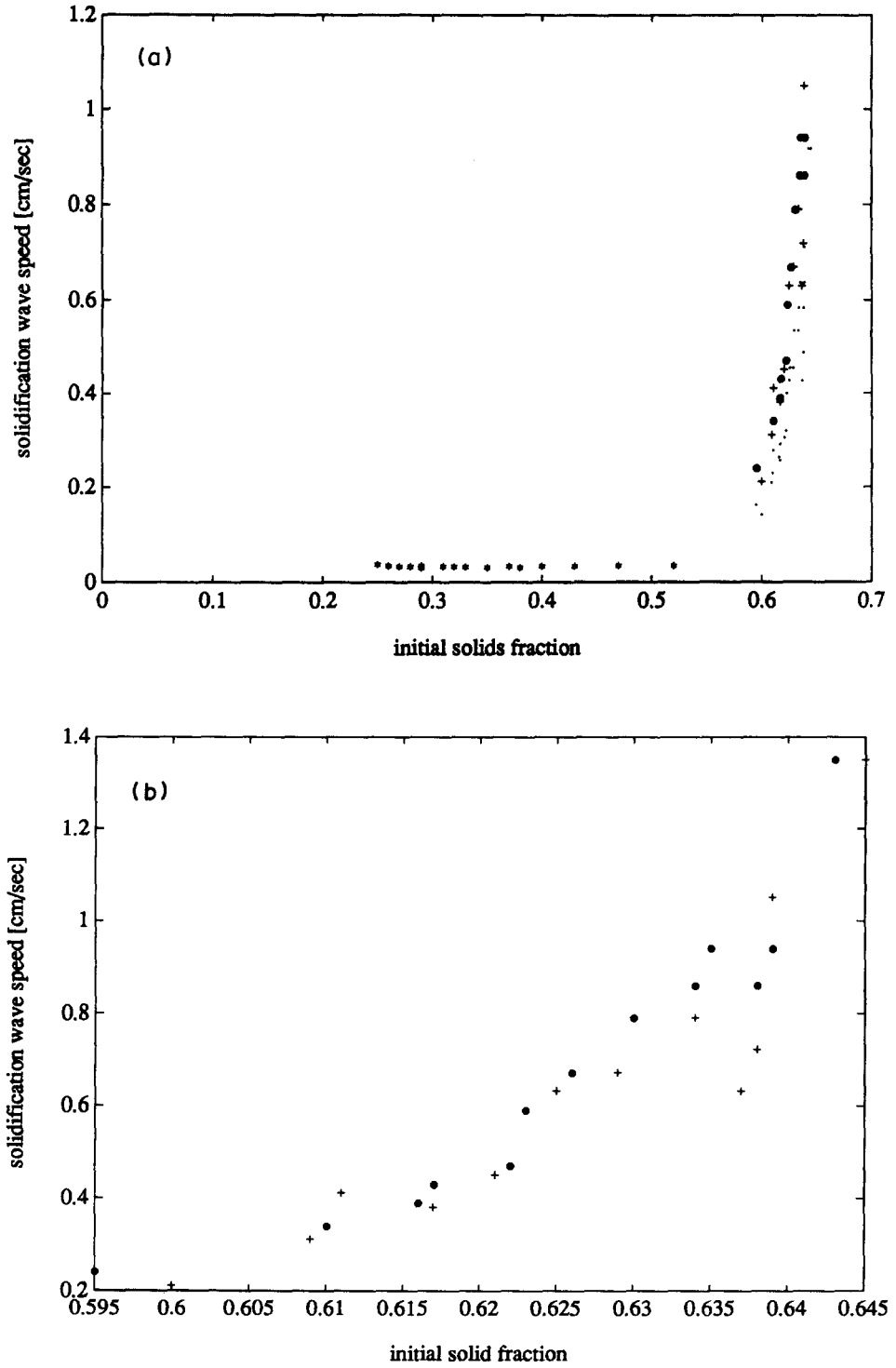

Figure 4. (a) Solidification wave speed measured visually for sedimentation ($v_0 = 0.25 - 0.52$) (*) and ultrasonically for mechanically induced liquefaction ($v_0 > 0.6$). Uncalibrated shock speeds (·) are shown for two series of liquefaction tests, and the corresponding calibrated values are shown as (+) and (●). Note the dramatic rise in the solidification wave speed at $v_0 > 0.6$. (b) The same two sequences of ultrasonically determined solidification wave speeds for mechanically induced liquefaction. These are shown as (+) and (●) as in figure 4(a).

under the normal stresses of the particles' own weight (Kytömaa 1991). While these effects would tend to result in deviations from the Kynch sedimentation theory, under the low stresses of the present experiments, they are considered to be negligible. The drift flux theory, which is based on the work by Kynch, provides a useful framework to predict the speed of concentration shocks using a steady-state empirical relation for the relative velocity between constituents in the absence of significant wall effects. According to this theory, the upward propagation speed of finite shocks, C, is given by the relation

$$C = j + \frac{\Delta j_{sj}}{\Delta v} = j + \frac{j_{sj}(v_0)}{\Delta v}, \qquad [1]$$

where j is the total volume flow of liquid and solids per unit cross-sectional area, and Δj_{sj} is the jump in the drift flux across the shock. Δj_{sj} equals the drift flux above the shock, $j_{sj}(v_o)$, as the two constituents do not move relative to one another in the settled region. Δv is the jump in solids fraction across the shock. The drift flux is the downward flux (volume flow/unit cross-sectional area) of solid particles relative to a plane moving at the total flux, j, or

$$j_{sj} = v(v_s - j), \qquad [2]$$

where $j = vv_s + (1 - v)v_l$. In this case $j = 0$ as the vessel has a solid bottom. It follows that

$$j_{sj} = (v_s - v_l)v(1 - v) = v_{sl}v(1 - v), \qquad [3]$$

where $v_{sl} = (v_s - v_l)$ is the mean relative velocity between species. The drift flux correlation developed by Richardson & Zaki (1954) (also described in Wallis 1969)

$$j_{sj} = v_\infty v(1 - v)^n \qquad [4]$$

conveniently predicts $j_{sj}(v_o)$ for the suspension above the interface. For the present system configuration, and a bed width of 5 cm, the R–Z correlation gives $n = 4.45$, while the terminal velocity, v_∞, of our 50 μm beads is 1.74 mm/s in water. Additional steady-state fluidization experiments were conducted for further confirmation and are shown in figures B1 and B2 in appendix B. These yielded $n = 4.55$ and $v_\infty = 1.77$ mm/s. This good agreement reflects the validity of the correlation.

The R–Z correlation can be substituted into [1] with $j = 0$, and using the measured initial and final concentrations, the internal wave speed can be predicted for the conditions of the visually studied sedimentation tests. It is important to note that $j_{sj}(v_0)$ is of the order of the terminal velocity of an isolated sphere at all concentrations near maximum packing, while the denominator in [1] is the difference in solids fraction across the shock. This quantity, Δv, is typically very small and is the cause of the fast solidification waves shown in figure 4. The jump in concentration is no more than a fraction of 1% and it is difficult to measure with much accuracy. Errors in measured Δv result in large errors in the calculated shock speeds. As the error in the measured speeds is much smaller than that in Δv, we use [1] to derive the increment in concentration that corresponds to the measured shock speeds, rather than comparing the measured speeds with calculated ones based on erroneous Δv values. The progressive increment in solids fraction is discussed further below.

3.3. Packing history of consecutive compaction events

The solids fraction of the packed bed was calculated from the measured bed heights for each sequence of liquefaction tests. A gradual increase in solids fraction from 0.6 to 0.65 was observed above which further compaction could no longer be detected. The bed heights were measured using a digital caliper accurate to 0.001″ (25 μm), while the mean particle diameter was 50 μm. For the small changes in bed height, at their smallest of the order of a few units of resolution, random error of the order of the particle diameter is present in these measurements. As measurements of wave speed are less prone to random error, these were used to predict the concentration change for comparison, using the drift flux model. The equation used to determine the increment in solids fraction is $\Delta v = j_{sj}(v_0)/C$. The calculated increments in solids fraction are shown in figure 5 for liquefaction and sedimentation experiments, in which the low initial solids fraction was achieved by fluidization. The liquefaction data showed a monotonic increase with each consecutive tap. The measured increment in v exhibits some scatter, but all points fall near the 45° line. The implied

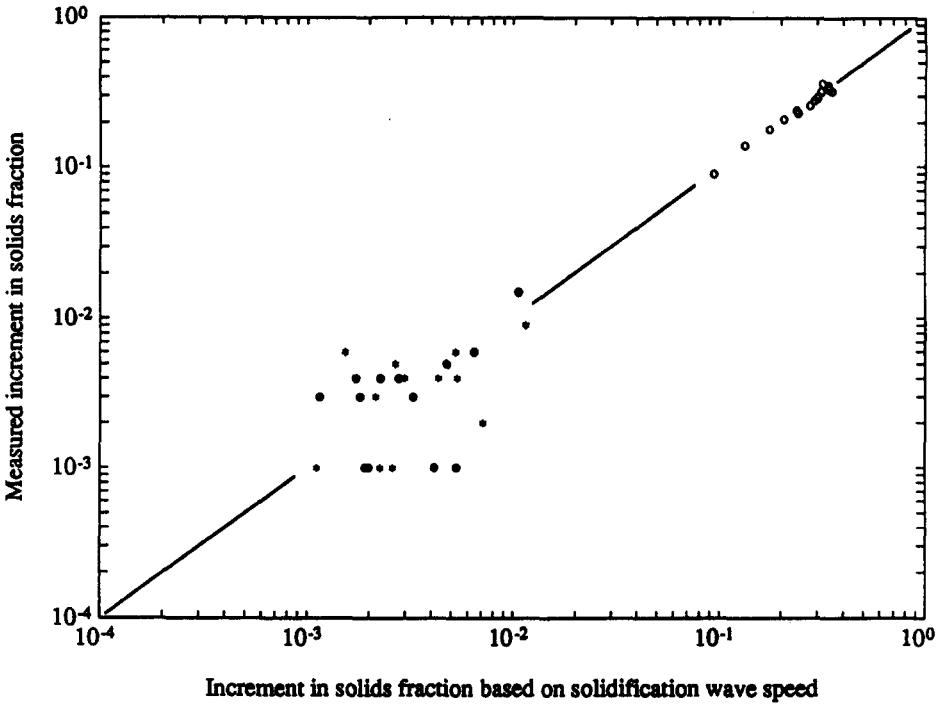

Figure 5. Calculated vs measured increments in solids fraction upon successive strikes of the packed bed for two sequences (* and ●). The calculated values are based upon the measured solidification wave speed. The high increments correspond to sedimentation tests from an initial fluidized state.

relationship between the solidification wave speed and the increment in solids fraction demonstrates the similarity between the solidification phenomenon and the theory of sedimentation. Unlike the direct measurements of Δv, the calculated values are relatively free of random scatter. These are shown in figure 6 as a function of v prior to each tap. The associated increment in solids loading gradually becomes smaller as the bed becomes more dense.

The lowest value of v for a settled bed in these experiments was 0.595, and most fluidized beds settled to $v \approx 0.60$. This agrees with similar measurements be Onoda & Liniger (1990), who used 250 μm glass spheres in water. These experiments indicate the path taken by the solids fraction as the bed is subjected to a series of manual taps under gravity, and its repeatability is surprisingly good. Under these conditions, the densification process ceased at $v = 0.645$. The meaning of the maximum packing fraction of 0.645, or the nature of figure 6 has implications for various processes where high density particulate beds are sought (e.g. filters, ceramic components), but quantitative answers will only be provided with the use of "calibrated taps."

4. DISCUSSION AND CONCLUSIONS

This study was motivated by the limited amount of information available on transient liquefaction of saturated cohesionless soils.

To this end, the feasibility of using clinical ultrasound was determined by first selecting the appropriate operating frequency for the present 50 μm glass bead/water system to ensure sufficient penetration as well as good spatial resolution using the results of Atkinson and Kytömaa (1992). The choice of 2.5 MHz proved to satisfy these conditions, and it was used to image sequences of mechanically induced liquefaction events. It was discovered that liquefied states could readily be distinguished from settled ones not on the basis of a subtle change in mean bulk properties but rather, by means of the inherent random fluctuations that exist in the liquefied state on the scale of tens of particle diameters. These were clearly visible in ultrasonic images. The moving difference between images spaced by 0.2 s was effectively used to distinguish the "frozen" appearance of settled states from the randomly fluctuating suspension.

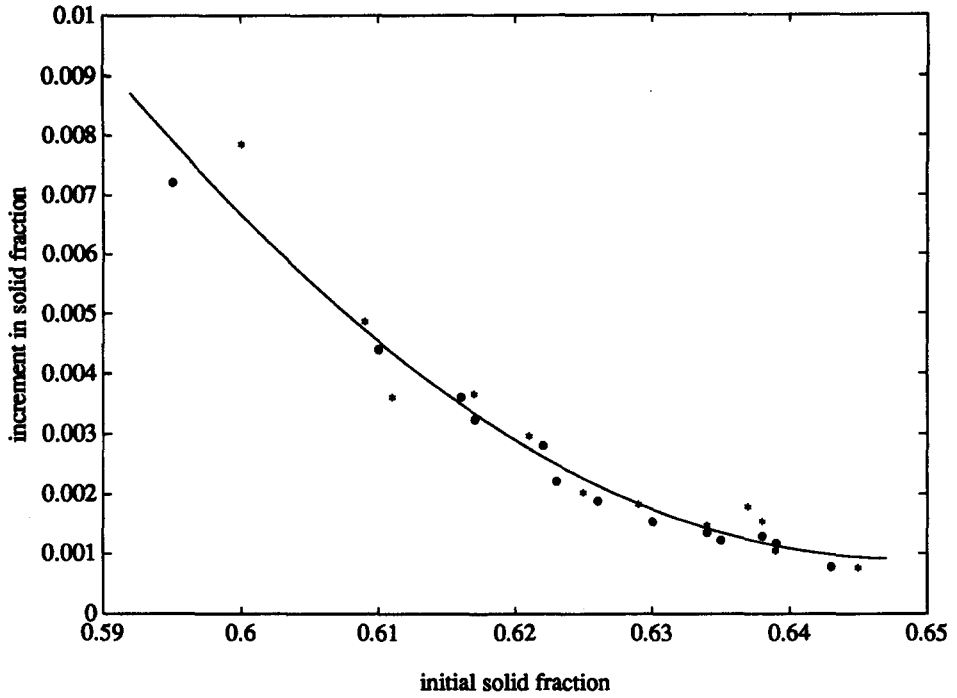

Figure 6. Calculated (* and ●) increments in solids fraction upon successive strikes of the packed bed, based upon the measured solidification wave speed. Each tap results in a progressively decreasing increment in solids fraction which ceases at $v = 0.645$. The quadratic best fit to these data is shown to make a good match, and to reach a minimum at $v \approx 0.65$.

It was found that the solidification process is analogous to sedimentation, and entails the upward propagation of a solidification shock below which the particles are settled at an elevated concentration. This is consistent with the phenomenological description of post-liquefaction pore pressure drop in centrifuge tests due to Scott (1986 a, b) although the latter were affected by significant elastic deformation of the settled region. Here, the shock was found to travel upward at speeds up to one order of magnitude higher than the terminal velocity of individual particles, which was conclusively shown to be the result of the small jump in solids fraction across the shock.

Clinical ultrasonic equipment is calibrated for biological tissue which has a sound speed and ultrasonic impedance that are only slightly above those of water, while the present materials have

Table 1. Numerical data of initial solid fraction and corrected solidification wave speed for the two sequences shown graphically

First sequence		Second sequence	
Initial solid fraction	Wave speed (cm/s)	Initial solid fraction	Wave speed (cm/s)
0.6000	0.2100	0.5950	0.2400
0.6090	0.3100	0.6100	0.3400
0.6110	0.4100	0.6160	0.3900
0.6170	0.3800	0.6170	0.4300
0.6210	0.4500	0.6220	0.4700
0.6250	0.6300	0.6230	0.5900
0.6290	0.6700	0.6260	0.6700
0.6340	0.7900	0.6300	0.7900
0.6370	0.6300	0.6340	0.8600
0.6380	0.7200	0.6350	0.9400
0.6390	1.0500	0.6380	0.8600
0.6450	1.3500	0.6390	0.9400
		0.6430	1.3500

higher values. The elevated speed of sound results in shrinkage of the radial scale, and the elevated impedance ($\approx 3 \times 10^6$ kg/m^2 s) of both the acrylic wall and the mixture cause refraction of the ultrasonic "fan" that distorts the circumferential dimension. To alleviate these dimensional distortions, a semi-empirical dynamic calibration procedure was developed to rescale the video image.

Video monitor measurements of the solidification wave speed were well matched by the drift flux model with the Richardson–Zaki correlation, using the measured initial and final solids fractions. This correlation was found adequate within experimental error. For better accuracy, modifications of the R–Z model have been put forward that perform better at high solid fractions. Furthermore, this model is based on the steady-state settling properties of the suspension, and does not account for unsteady effects such as inertia. While the model proved to be consistent with the data, such effects can be expected to become important as the shock speed rises above a critical magnitude that would result in high accelerations. Finally, although random fluctuations were visible in the suspension, it is interesting to note that diffusion was never observed to play a significant role in increasing the "width" of the shock.

The medical field continues to provide innovations in non-invasive instrumentation much of which stands to have an impact on multicomponent flow studies due to their common features with biological systems. By addressing a task that has not been earlier achieved, this study demonstrates that ultrasound can effectively be used for real time imaging (30 Hz) in very dense suspensions and porous media, with a spatial resolution of the order of 10 particle diameters or 10 × the characteristic pore dimension.

REFERENCES

ATKINSON, C. M. & KYTÖMAA, H. K. 1992 Ultrasonic wave speed and attenuation in suspensions. *Int. J. Multiphase Flow* **18,** 577–592.

ATKINSON, C. M. & KYTÖMAA H. K. 1993 Acoustic properties of solid–liquid mixtures and the limits of ultrasound diagnostics—I: Experiments. *J. Fluids Engng* **115,** 665–675.

AUZERAIS, F. M., JACKSON, R. & RUSSELL, W. B. The resolution of shocks and the effects of compressible sediments in transient settling. *J. Fluid Mech.* **195,** 437–462.

AUZERAIS, F. M., JACKSON, R. RUSSELL, W. B. & MURPHY, W. F. 1990 The transient settling of stable and flocculated dispersions. *J. Fluid Mech.* **221,** 613–639.

GEISER, E. A. 1988 Echocardiography: Physics and instrumentation. In *Cardiac Imaging* (Edited by MARCUS, M. L., SCHELBERT, H. R., SKORTON, D. J. & WOLF, G. L.), Chap. 17. Saunders, Philadelphia, PA.

HEWLETT–PACKARD, *Sonos* 1000 *Instruction Manual.* Hewlett–Packard, Andover, MA, U.S.A.

KYNCH, G. J. 1952 A theory of sedimentation. *Trans. Faraday Soc.* **48,** 166–176.

KYTÖMAA, H. K. 1990 Propagation and structure of solidification waves in concentrated suspensions. *Mech. Mater.* **9,** 205–215

NATIONAL RESEARCH COUNCIL 1985 *Liquefaction of Soils During Earthquakes.* Prepared by the Committee on Earthquake Engineering, Commission on Engineering and Technical Systems, National Academy Press.

ONODA, G. Y. & LINIGER, E. G. 1990 Random loose packings of uniform spheres and the dilatancy onset. *Phys. Rev. Lett.* **64,** 2727–2730.

RICHARDSON, J. F. & ZAKI, W. N. 1986 *Trans. Inst. Chem. Engrs* **32,** 35–53.

SCOTT, R. F. 1986a Soil properties from centrifuge liquefaction tests. *Mech. Mater.* **5,** 199–205.

SCOTT, R. F. 1986b Solidification and consolidation of a liquefied sand column. *Soils Foundations, Jap. Soc. Soil Mech. Foundation Engng* **26,** 23–31.

TERZAGHI, K. 1943 *Theoretical Soil Mechanics.* Wiley, New York.

TILLER, F. M. 1981 Revision of Kynch sedimentation theory. *AIChE Jl* **27,** 823–829.

TURNEY, M. Experimental investigation of suspension mechanics using magnetic resonance imaging. M.Sc. thesis, Department of Chemical Engineering, U. C. Davis, CA, U.S.A.

WALLIS, G. B. 1969 *One-dimensional Two-phase Flow*, pp. 190–204. McGraw–Hill, New York.

APPENDIX A

Dynamic Calibration of the Veritcal Scale in Ultrasonic Images

The solidification wave speed can conveniently be written in terms of the drift flux at the initial solids fraction and the measured change in solids fraction across the solidification interface using [2]. Under conditions where the change in concentration Δv_i is very small, the wave speed becomes large as is apparent in figure 3. Since the drift flux is known for the initial solids fraction, the change in solids fraction over each liquefaction/solidification event can be calculated from the measured wave speed. By adding up all consecutive increments in solids fraction $\Sigma_{i=1}^{l} \Delta v_i$. where l is the number of liquefaction events, we arrive at the total change in solids fraction over the sequence of liquefaction tests, which must agree with the measured total change. A single calibration scale factor ξ is introduced to adjust the uncalibrated video length scale to satisfy this required equality. Using this calibration parameter the actual wave speed can be written $C_{\text{actual}} = \xi C_{\text{meas}}$. Equating the calculated and measured total change in solids fraction gives

$$\sum_{i=1}^{l} \Delta v_i = \sum_{i=1}^{l} \left(\frac{j_{sj}(v_0)}{\xi C_{\text{meas.}}} \right)_i = \sum_{i=1}^{1} \Delta v_{\text{meas.}} \qquad \text{[A1]}$$

This yields the equation for ξ:

$$\xi = \sum_{i=1}^{l} \left(\frac{j_{sj}(v_0)}{C_{\text{meas.}}} \right)_i \Big/ \sum_{i=1}^{1} \Delta v_{\text{meas.}} \qquad \text{[A2]}$$

This calibration procedure uses all the measured data and therefore is not susceptible to the error in each measurement, which as the raw data shows is notable. It must be noted that this calibration makes use of the R–Z correlation which was only validated up to $v \approx 0.52$. Some error may be introduced by the extension of the model to higher values of v, although the error is suspected to be small compared to the prior discrepancy due to a lack of a calibrated length scale. For three sequences of measurements consisting of a total of 38 individual tests, the calibration factor was found to be 1.38, 1.49 and 1.56. Their average of $\xi = 1.47$ was adopted as the calibration factor used to adjust the data.

APPENDIX B

Drift Flux in Steady Fluidization

Empirical confirmation fo the drift flux model was obtained from steady fluidization experiments with a known volume of solids. These were conducted by adjusting the upward fluidizing liquid flow rate, and measuring it by collecting and measuring the volume flow over a prescribed period. The bed height, h, was also measured using a digital caliper accurate to 0.001″ (25 μm), The solids fraction, v, was calculated from the bed height. In steady-state fluidization, the mean solids velocity is zero ($v_s = 0$), hence the drift flux can be determined from

$$j_{sj} = \frac{Qv}{A}. \qquad \text{[B1]}$$

To determine the two coefficients in the R–Z model [5], namely the terminal velocity, v_∞, and the exponent n, the data was plotted with log–log axes using j_{sj}/v as the ordinate and $(1 - v)$ as the abscissa. The data fall on a line which has a slope of n and a y-intercept of v_∞. Linear regression of the data shown in figure B1 yielded the values

$$n = 4.55 \quad \text{and} \quad v_\infty = 0.177 \text{ cm/s}.$$

Figure B2 shows the measured fluidization drift flux, j_{sj}, the corresponding best fit curve, as well as the R–Z curve and the best fit derived from the visual sedimentation experiments in section 3. The fact that all these curves are very close to one another indicates that this model is indeed applicable for the present unsteady application.

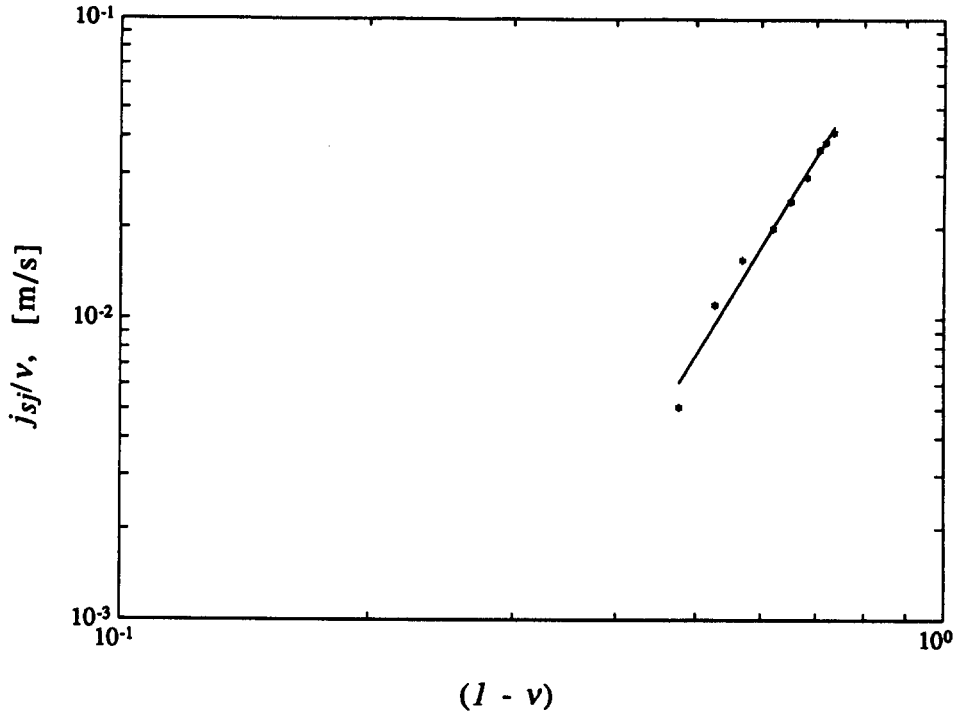

Figure B1. This plot is used to determine the best fit values of n and v_∞ from measurements of fluidization solids fraction and liquid flow rate. The slope yields $n = 4.55$ and the y-intercept yields $v_\infty = 0.177$ cm/s.

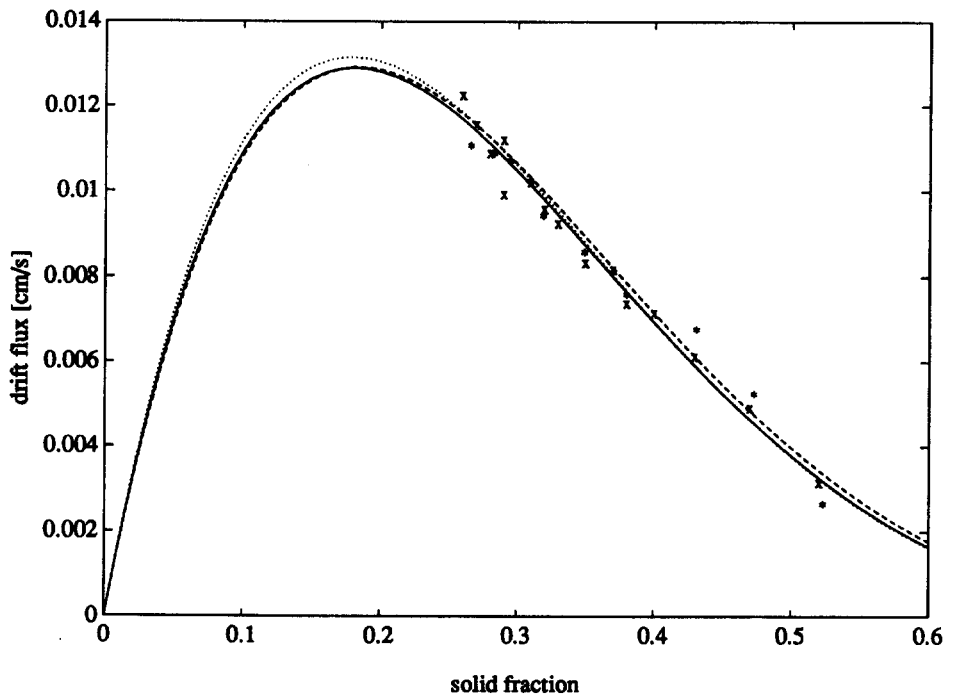

Figure B2. Drift flux curves for 50 μm glass beads in water based on fluidization tests (—), sedimentation tests (· · ·) and the Richardson–Zaki correlation (– – –). All remarkably close to one another. The experimental points (×) correspond to sedimentation tests and points (*) correspond to fluidization tests.